

Role of seed layer in growing atomically flat TiTe₂/Sb₂Te₃ heterostructure thin films at the wafer scale

Chao Nie¹, Xueyang Shen¹, Junying Zhang¹, Chenyu Wen¹, Yuxin Du¹, Yazhi Xu², Riccardo Mazzarello³, En Ma¹, Xiaozhe Wang^{1,*}, Wei Zhang^{1,*}, Jiang-Jing Wang^{1,*}

¹Center for Alloy Innovation and Design (CAID), State Key Laboratory for Mechanical Behavior of Materials, Xi'an Jiaotong University, Xi'an 710049, China.

²Department of Applied Physics, Chang'an University, Xi'an 710049, China.

³Department of Physics, Sapienza University of Rome, Rome 00185, Italy.

Emails: wangxiaoze@xjtu.edu.cn, wzhang0@mail.xjtu.edu.cn, j.wang@xjtu.edu.cn

Abstract:

Chalcogenide phase-change materials (PCMs) are a leading candidate for advanced memory and computing applications. Epitaxial-like growth of chalcogenide thin films at the wafer scale is important to guarantee the homogeneity of the thin film but is challenging with magnetron sputtering, particularly for the growth of phase-change heterostructure (PCH), such as TiTe₂/Sb₂Te₃. In this work, we report how to obtain highly textured TiTe₂/Sb₂Te₃ heterostructure thin films with atomically sharp interfaces on standard silicon substrates. By combining atomic-scale characterization and *ab initio* simulations, we reveal the critical role of the Sb₂Te₃ seed layer in forming a continuous Si-Sb-Te mixed transition layer, which provides a wafer-scale flat surface for the subsequent epitaxial-like growth of TiTe₂/Sb₂Te₃ thin film. By gradually reducing the thickness of the seed layer, we determine its critical limit to be ~2 nm. Non-negligible in-plane tensile strain was observed in the TiTe₂ slabs due to the lattice mismatch with the adjacent Sb₂Te₃ ones, suggesting that the chemical interaction across the structural gaps in the heterostructure is stronger than a pure van der Waals interaction. Finally, we outline the potential choices of chalcogenides for atomically flat seed layers on standard silicon substrates, which can be used for wafer-scale synthesis of other high-quality PCM or PCH thin films.

Keywords: phase-change heterostructure, seed layer, thin film, atomic characterizations, TiTe₂/Sb₂Te₃

1. Introduction:

Chalcogenide phase-change materials (PCMs) are one of the leading candidates for non-volatile memory and neuromorphic in-memory computing applications [1-10]. The most important family of PCM consists of the Ge-Sb-Te alloys along the GeTe-Sb₂Te₃ pseudo-binary line [11-19], e.g. Ge₂Sb₂Te₅ (GST), which has been extensively used in electronic, photonic as well as hybrid optoelectronic devices [20-28]. The basic working principle is the large contrast in electrical resistance or optical transmission between the crystalline and amorphous phases of PCM for memory encoding [1]. Given its metastable nature, the amorphous phase undergoes spontaneous structural relaxation, causing a steady increase in electrical resistance with time, known as the resistance drift [29-32]. For binary storage, this aging effect is not a serious issue, as the contrast window is enlarged instead of reduced with time. But for the multilevel programming scheme adopted in neuromorphic devices, the drift issue is a major hindrance for high-precision encoding of multiple resistance states [33-35].

The structural origin of the resistance drift in amorphous PCMs stems from the disappearance of structural defects that are generated during the rapid cooling process and the reinforcement of Peierls-like distortions between pairs of octahedral bonds with time [36-39]. Scaling down the film thickness to exploit volume effects [40-43] or alloying PCM with impurities can help reduce the drift coefficient effectively [44-47]. Another promising approach to suppress drift is based on heterostructures composed of alternating thin layers of two different PCMs or of a PCM and a confinement material (CM). Such heterostructures are typically grown by heterogeneous sputtering or molecular beam epitaxy. Besides the low drift, they also offer low switching energy and fast switching speed. Prominent examples include the GeTe(GST)/Sb₂Te₃ [48-57] superlattice heterostructures, which are made of two standard PCMs with similar melting point, and the TiTe₂/Sb₂Te₃ phase-change heterostructures (PCH) [58-63]. In the latter, TiTe₂ serves as CM due to its much higher melting point than Sb₂Te₃, effectively reducing the drift coefficient of the PCM layers. More heterostructure combinations were predicted [64] and developed [65-68] for memory applications with CM = TiTe₂, MoTe₂, NiTe₂ or HfTe₂, and PCM = GeTe, GST, Ge₄Sb₆Te₇ or Ta_xSb₂Te₃.

For practical use, it is important to form sharp interfaces between the CM layers and PCM layers during growth. Otherwise, accumulation of structural defects at the interfaces upon extensive cycling could turn the PCM into conventional transition metal doped alloys, causing device degradation [58, 59]. In this work, we report how to deposit TiTe₂/Sb₂Te₃ heterostructure thin films with atomically sharp interfaces at the wafer scale. The key to obtaining high-quality heterostructure thin films relies on the quality of the seed layer deposition and the *in situ* heating during subsequent co-sputtering of the heterostructure. We determine the critical (minimum) thickness of the seed layer required to ensure the formation of sharp interfaces on a standard silicon substrate, and provide in-depth understanding of this interface region via atomic-scale structural characterization experiments and *ab initio* calculations. We also find that the TiTe₂ crystal lattice is under non-negligible tensile strain due to the lattice mismatch with crystalline Sb₂Te₃. At last, we provide guidelines on the choice of seed layer that can guarantee highly textured thin film deposition.

2. Experimental and simulation details

The TiTe₂/Sb₂Te₃ heterostructure thin films were deposited on silicon wafers by magnetron sputtering (AJA, Orion-8). The silicon wafers were cleaned by sonication in acetone, ethanol, and deionized water

for 10 min, respectively, and then baked at 80°C for 30 minutes. The base pressure in the deposition chamber was maintained at $\sim 1 \times 10^{-7}$ Torr. The Sb_2Te_3 layers were deposited using a Sb_2Te_3 (99.99%) target at a pressure of 3 mTorr, and the TiTe_2 layers were deposited by co-sputtering with Ti (99.995%) and Te (99.99%) targets at a pressure of 4.7 mTorr. The cross-section specimens of the $\text{TiTe}_2/\text{Sb}_2\text{Te}_3$ thin films were prepared using a FEI Helios NanoLab 600i focus ion beam (FIB) system with a Ga ion beam at 30 kV beam energy, and were thinned and polished at 5 kV / 20 pA and 2 kV / 10 pA, respectively. The spherical aberration corrected scanning transmission electron microscopy (STEM) high-angle annular dark-field (HAADF) and energy dispersive X-ray (EDX) mapping experiments were performed on a JEM-ARM300F2 STEM with a probe aberration corrector, operated at 300 kV. The high-resolution transmission electron microscopy (HRTEM) and EDX experiments were performed on a Talos-F200X operated at 200 kV. The atomic force microscopy (AFM) experiments were measured using a SPM-9700HT. The X-ray diffraction (XRD) experiments were performed by a Bruker D8 ADVANCE with $\text{CuK}\alpha$ radiation ($\lambda = 1.54056$) in the 2θ range $5^\circ\sim 60^\circ$ with the scanning step size of 0.02° . The Raman spectra were collected by using a Renishaw inVia Qontor Raman microscope with a solid-state 532 nm laser for the excitation. The laser power was set to 0.25 mW, and the exposure time was 1 s with 100 cycles. Density functional theory (DFT) calculations were carried out using the Vienna Ab-initio Simulation Package (VASP) code [69]. The Perdew-Burke-Ernzerhof (PBE) functional [70], the projector augmented plane-wave (PAW) pseudopotentials [71], and the Grimme's D3 dispersion correction [72] were applied in the calculations. An energy cutoff of 500 eV was used. We constructed $2 \times 2 \times 5$ TiTe_2 and $2 \times 2 \times 1$ Sb_2Te_3 supercells that both contained 60 atoms, and used k-point mesh of $9 \times 9 \times 2$ points used to sample the Brillouin zone. The Löwdin charges were calculated using the LOBSTER code [73-75].

3. Results and discussion

We deposited several $\text{TiTe}_2/\text{Sb}_2\text{Te}_3$ PCH thin films on $7 \text{ cm} \times 7 \text{ cm}$ silicon wafers following the procedure shown in Fig. 1a. Before deposition, the silicon substrate was cleaned using Ar-plasma etching with radio frequency at ~ 35 Watt over 30 minutes in the high vacuum sputtering chamber. This cleaning process is needed to remove the native oxides on top of the substrate, and is frequently termed as the reverse sputtering process [76-78]. As soon as the etching was completed, a ~ 5 nm Sb_2Te_3 seed layer was deposited at room temperature. Next, the substrate was heated at $\sim 280^\circ \text{C}$ for 60 min to fully crystallize the Sb_2Te_3 seed layer, forming a trigonal phase with ordered Sb_2Te_3 quintuple-layer (QL) blocks (each QL has a thickness of ~ 1 nm) [79-81]. Subsequently, a PCH unit made of a ~ 5 nm TiTe_2 slab, corresponding to $\sim 7\text{--}8$ TiTe_2 trilayer (TL) blocks, followed by a ~ 5 nm Sb_2Te_3 slab, were deposited via alternate sputtering of the Sb_2Te_3 , Ti and Te targets under the *in situ* heating condition. In total, four PCH units were deposited. As the last step, the PCH thin film with a thickness of ~ 45 nm (including the seed layer) was annealed at 280°C for another 30 min, and was naturally cooled to room temperature in the high vacuum chamber. The whole thin film was covered with a ~ 10 nm-thick ZnS-SiO₂ capping layer to prevent oxidation. The cross-sectional structural properties and elemental distributions of this $\text{TiTe}_2/\text{Sb}_2\text{Te}_3$ thin film were characterized by combining the HRTEM with EDX experiments. As shown in Fig. 1b, the HRTEM image provides an overview of the PCH thin film, which has well-aligned lattice fringes parallel to the substrate. In the corresponding EDX mapping, the Ti (red) and Sb (green) signals are well separated, while the Te (blue) signal is uniformly distributed throughout the PCH thin film. Only the Sb and Te signals were detected within the bottom ~ 5 nm region in contact with the substrate.

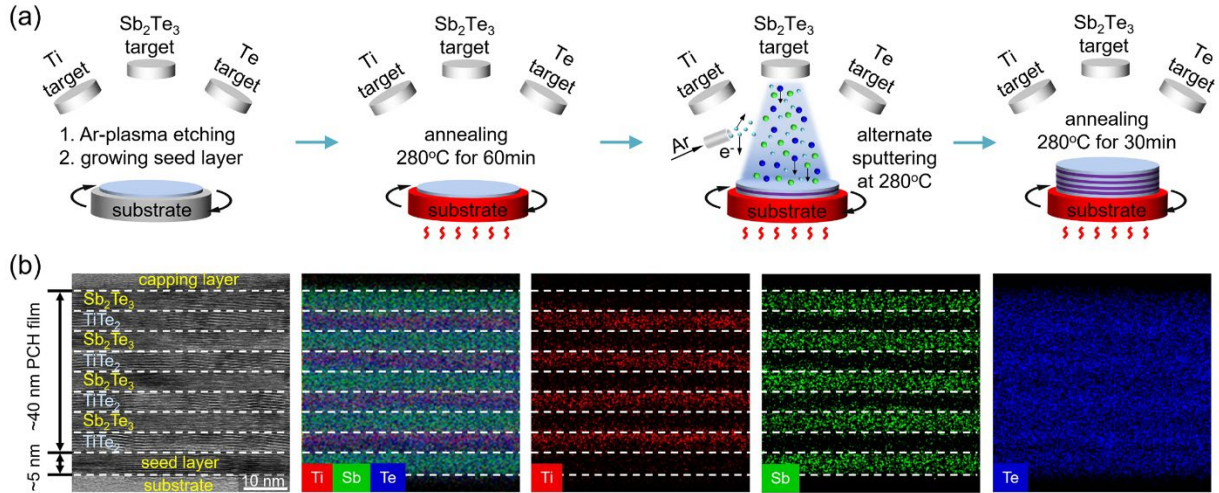


Fig. 1 The deposition procedure and characterization of the $\text{TiTe}_2/\text{Sb}_2\text{Te}_3$ thin film. (a) The schematic diagrams of the deposition process in four steps. (b) The HRTEM and EDX mapping images of the PCH thin film.

The epitaxial-like growth of the PCH thin film depends on the quality and out-of-plane texture of the Sb_2Te_3 seed layer. In Fig. 2, we characterized the surface morphology of a seed layer and a full PCH thin film. The optical images of the two thin films on the silicon wafers are presented in Fig. 2a and 2c. We selected 16 uniformly distributed regions across the two thin films and measured the surface roughness of each region by using AFM. For each AFM scan, the size of the measured region was set to $2\ \mu\text{m} \times 2\ \mu\text{m}$. Fig. 2b presents the AFM images of six regions of the seed-layer sample (the remaining 10 AFM images are included in Fig. S1a of the supplementary material). The respective root-mean-square roughness R_q values provided in the figure range from $\sim 4.41\ \text{\AA}$ to $\sim 5.17\ \text{\AA}$, indicating a highly smooth surface. The 16 AFM images of the PCH thin films are shown in Fig. 2d and Fig. S1b. The R_q values range from $\sim 6.50\ \text{\AA}$ to $\sim 7.50\ \text{\AA}$, which is slightly broader than that of the seed layer but is still smaller than the thickness of a single Sb_2Te_3 QL block. Therefore, we conclude that we have obtained a high-quality PCH thin film with smooth surface.

We carried out XRD and Raman spectroscopy experiments to investigate the structural properties of the obtained PCH thin films. We also prepared pristine Sb_2Te_3 and TiTe_2 thin films of $\sim 45\ \text{nm}$ thickness for comparison, for which a $\sim 5\ \text{nm}$ Sb_2Te_3 seed layer was used consistently. Fig. 3a and Fig. S2a show the measured XRD patterns at 16 locations of the PCH thin film. No obvious difference can be observed in these XRD curves. In comparison with the two pristine thin films, the PCH thin film exhibited a series of (001)-oriented diffraction peaks, namely, the (003), (006), (009), (0015) and (0018) peaks of the Sb_2Te_3 slabs, and the (001) and (002) peaks of the TiTe_2 slabs. Note that the Sb_2Te_3 (009) and TiTe_2 (002) peaks overlap due to their close peak locations at $2\theta \sim 26.3^\circ$ and 27.0° , leading to a smaller shoulder in the primary peak of the PCH thin film. These well-defined (001)-oriented diffraction patterns confirm the epitaxial-like growth with out-of-plane texture across the entire wafer.

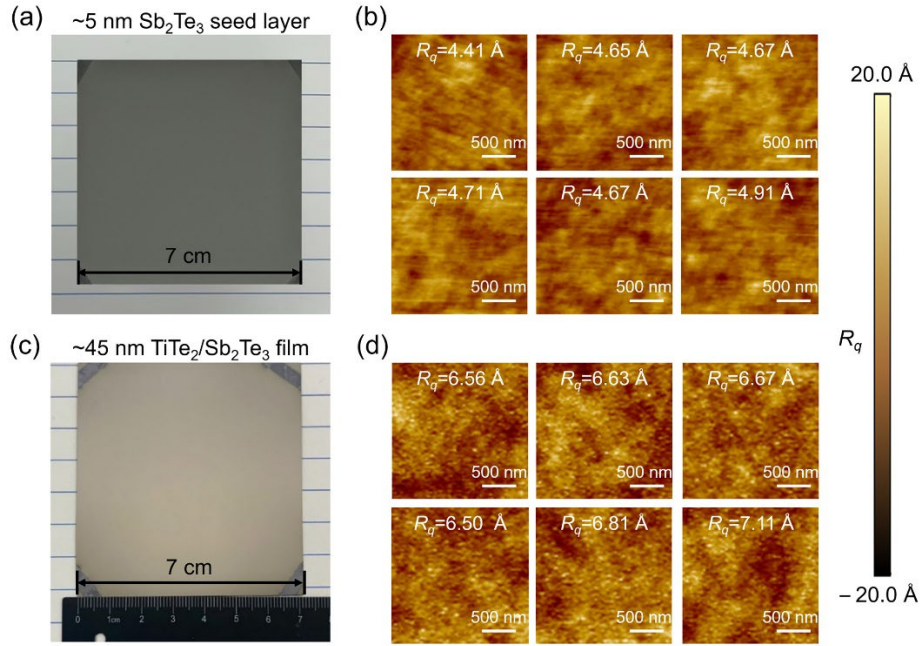


Fig. 2 Surface morphology characterization of the seed layer and the PCH thin film. (a) The optical image of the Sb_2Te_3 seed layer with a thickness of ~ 5 nm on a silicon wafer. (b) The AFM images taken at 6 different locations on the surface of the seed layer. (c) The optical image of the $\text{TiTe}_2/\text{Sb}_2\text{Te}_3$ thin film on a silicon wafer. (d) The AFM images taken at 6 different locations on the surface of the PCH thin film. R_q is the measured root-mean-square roughness.

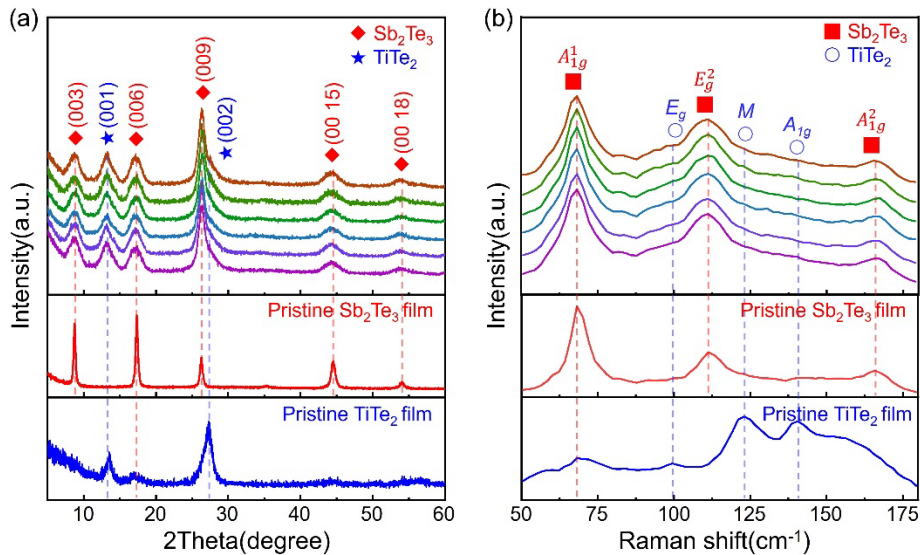


Fig. 3 XRD and Raman characterizations. The (a) XRD and (b) Raman characterizations carried out on various locations of the PCH thin film. The XRD and Raman curves of the pristine Sb_2Te_3 thin film and pristine TiTe_2 thin film are shown for comparison.

Fig. 3b and Fig. S2b present the Raman spectra measurements of the three thin films within a range of $50\text{--}180\text{ cm}^{-1}$ using a 532 nm solid-state excitation laser. The measured local Raman spectra at 16 locations of the PCH thin film show three major peaks. By comparing with pristine Sb_2Te_3 [82–84],

the three vibrational modes are identified as an out-of-plane mode A_{1g} (1) at $\sim 68.2 \text{ cm}^{-1}$, an in-plane mode E_g (2) at $\sim 111.3 \text{ cm}^{-1}$ and a second out-of-plane mode A_{1g} (2) at $\sim 165.8 \text{ cm}^{-1}$ for the PCH thin film. For the pristine TiTe_2 thin film, three major vibrational modes [85] were found at $\sim 101.5 \text{ cm}^{-1}$ for E_g , $\sim 124.9 \text{ cm}^{-1}$ for M and $\sim 142.4 \text{ cm}^{-1}$ for A_{1g} , respectively. However, these TiTe_2 -related vibrational modes were not visible in the PCH thin film due to the much weaker Raman response. The highly consistently XRD patterns and Raman spectra across the entire $\text{TiTe}_2/\text{Sb}_2\text{Te}_3$ thin film are indicative of wafer-scale uniformity.

Next, we conducted STEM-HAADF imaging experiments to gain a better understanding of the atomic interfaces between TiTe_2 and Sb_2Te_3 in the heterostructure thin film. Fig. 4 presents the HAADF images of the pristine Sb_2Te_3 , pristine TiTe_2 and $\text{TiTe}_2/\text{Sb}_2\text{Te}_3$ thin films in the $[01\bar{1}0]$ direction. The brightness of each spot is roughly proportional to Z^2 , where Z represents the average atomic number of the atomic column along the incident direction of the electron beam [86]. The atomic layers in the Sb_2Te_3 blocks exhibit uniform image intensity, owing to the comparable atomic number of Sb ($Z=51$) and Te ($Z=52$). In contrast, the central atomic layer of the TiTe_2 blocks displays markedly reduced intensity due to the much smaller atomic number of Ti ($Z=22$). The size of the Sb_2Te_3 block in the pristine thin film and in the heterostructure thin film is comparable, but for the TiTe_2 blocks, the in-plane atomic spacing is enlarged from $\sim 3.77 \text{ \AA}$ in the pristine thin film to $\sim 3.86 \text{ \AA}$ in the PCH thin film. This in-plane expansion indicates that the lattice mismatch between Sb_2Te_3 and TiTe_2 induces a $\sim 2.4\%$ tensile strain in the TiTe_2 slabs of the PCH thin film. Similar behavior was observed in $\text{GeTe}/\text{Sb}_2\text{Te}_3$ thin films, where the tensile strain could reach $\sim 1.6\%$ in the GeTe slab as compared to bulk GeTe [87]. The observation of lattice expansion in the TiTe_2 slab suggests that the alternately stacked Sb_2Te_3 and TiTe_2 slabs are connected not only by pure van der Waals forces but also additional chemical interaction across the structural gaps. Therefore, the structural gaps in the $\text{TiTe}_2/\text{Sb}_2\text{Te}_3$ PCH should also be regarded as “vdW-like” gaps rather than pure vdW gaps, similar to those in $\text{GeTe}/\text{Sb}_2\text{Te}_3$ heterostructures, and those in trigonal bulk Sb_2Te_3 and GST [87-89]. In a recent work, we revealed the critical role of weak chemical interactions across the vdW-like gaps in stabilizing metavalent bonding (MVB) [90-93] in trigonal Sb_2Te_3 and GST, and explained how to tailor the degree of this in-gap interaction for altering the optical properties via uniaxial strain along the out-of-plane direction [94]. Although pristine TiTe_2 is regarded as a vdW material like other transition metal dichalcogenides [95], the inter-slab coupling can be significantly increased by co-sputtering with MVB-type layered solids, which induces in-plane strain affecting the electronic structure [96-98].

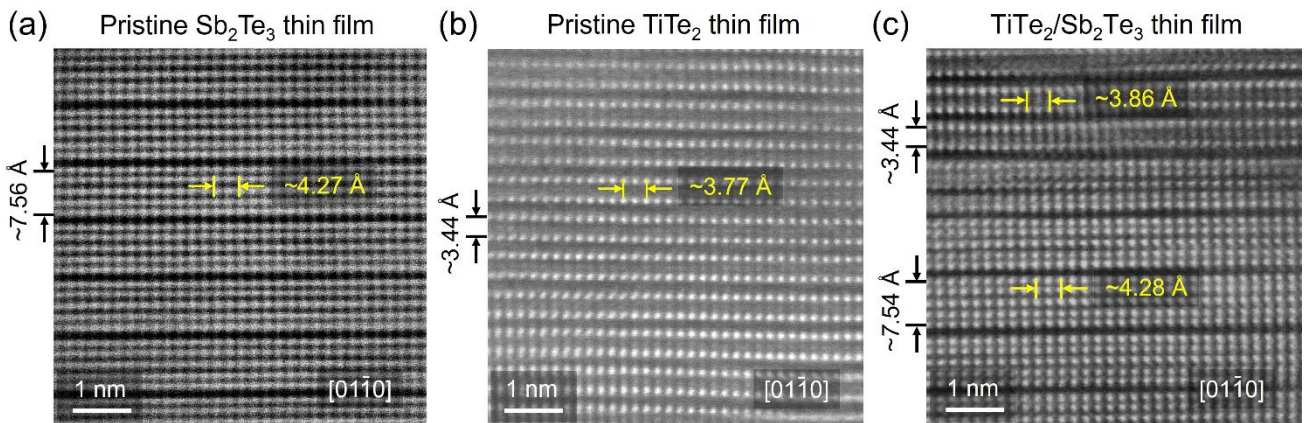


Fig. 4 Atomic-scale characterization of the lattice parameters along the $[01\bar{1}0]$ direction. The HAADF images of (a) the pristine Sb_2Te_3 thin film, (b) the pristine TiTe_2 thin film and (c) the $\text{TiTe}_2/\text{Sb}_2\text{Te}_3$ thin film.

The synthesis of the PCH thin film with wafer-scale uniformity is rendered possible by high-quality deposition of the seed layer. The HRTEM image in Fig. 5a shows an overall view of the multiple interfaces between different layers. We focus on the two interfaces indicated by the red and blue arrows, the corresponding atomic-scale HAADF images are shown in Fig. 5b and Fig. 5c. We used a standard silicon substrate with the $\langle 100 \rangle$ crystal orientation that was naturally covered with a $\sim 4\text{--}5$ nm SiO_2 layer. The initial Ar-plasma etching only removed native oxygen at the topmost of the substrate, not the full SiO_2 layer. The HAADF image (Fig. 5c) and the corresponding EDX maps (Fig. 5d–h) revealed a mixed Si-Sb-Te region of ~ 2 nm with no clear atomic columns except for the top three Sb-Te atomic layers. Above this transition region, we observed ordered Sb_2Te_3 QL blocks of the seed layer. Clearly, the ordered QL blocks are not directly contacted with the Si-100 surface. This transition region was formed because we conducted deposition of the Sb_2Te_3 seed layer immediately after Ar-plasma etching of the substrate. This procedure resulted in an amorphous Si layer of $\sim 2\text{--}3$ nm [76–78] with gradually reduced density from the substrate towards the seed layer (Fig. 5g), and the Si atoms intermixed with the subsequent sputtered Sb and Te atoms. It is important to note that the Ar-plasma etching process cannot be subjected to *in situ* heating, which markedly increases the probability of re-forming SiO_2 . In such a case it is no longer feasible to obtain a flat seed layer for high-quality growth of PCH thin films (Fig. S3).

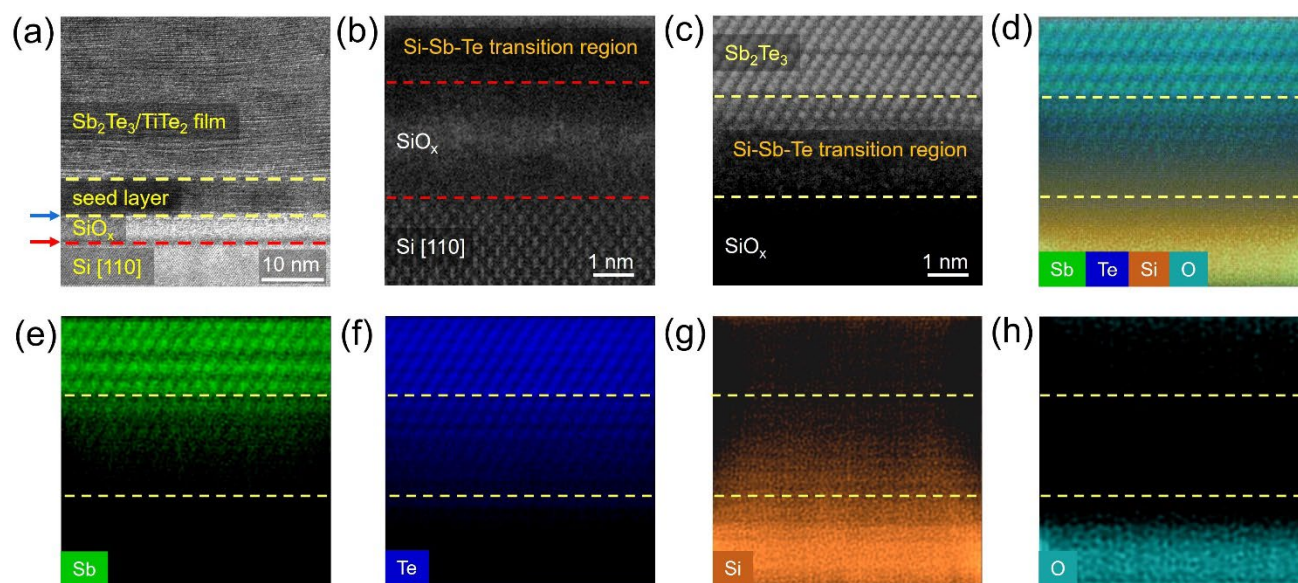


Fig. 5 Structural and elemental characterizations of the $\text{TiTe}_2/\text{Sb}_2\text{Te}_3$ thin film. (a) The large-scale HRTEM image of the multiple interfaces between the PCH thin film and the silicon substrate. (b) and (c) The atomic-resolution HAADF images of the interfaces marked by the red and yellow arrows in (a). (d)-(h) The corresponding EDX mapping of the transition region shown in (c).

The atomic-scale characterization of the seed layer suggests that its thickness t_s (Sb_2Te_3) can be further optimized. We repeated the sputtering process shown in Fig. 1a but reduced t_s (Sb_2Te_3) to ~ 2 nm, ~ 1 nm and finally 0 nm. In the latter case, the first ~ 5 nm TiTe_2 layer served as the seed layer. The HRTEM measurements showed that the PCH thin film with the ~ 2 nm Sb_2Te_3 seed layer exhibited well-aligned lattice fringes parallel to the substrate, as indicated by the white arrows in Fig. 6a. In the other two cases, the lattice fringes of the PCH thin films were no longer flat and smooth, as shown in Fig. 6b and Fig. 6c. The atomic-scale HAADF images of the seed layer region are shown in Fig. 6d-f for the three

PCH thin films. The first PCH thin film showed a similar Si-Sb-Te transition region with top 2–3 ordered Sb or Te atomic layers and a full Sb_2Te_3 QL block, consistent with that in the PCH thin film with $t_s(\text{Sb}_2\text{Te}_3) \sim 5$ nm. However, the transition region in the other two PCH thin films failed to promote the formation of well-ordered atomic layers at the top edge. Therefore, the critical minimum thickness of the seed layer is ~ 2 nm for Sb_2Te_3 to generate a flat surface, i.e., a full intact Sb_2Te_3 QL block, for the subsequent growth of high-textured thin films on top. However, it is less suitable to use TiTe_2 as the seed layer, as sketched in Fig. 6 g-i.

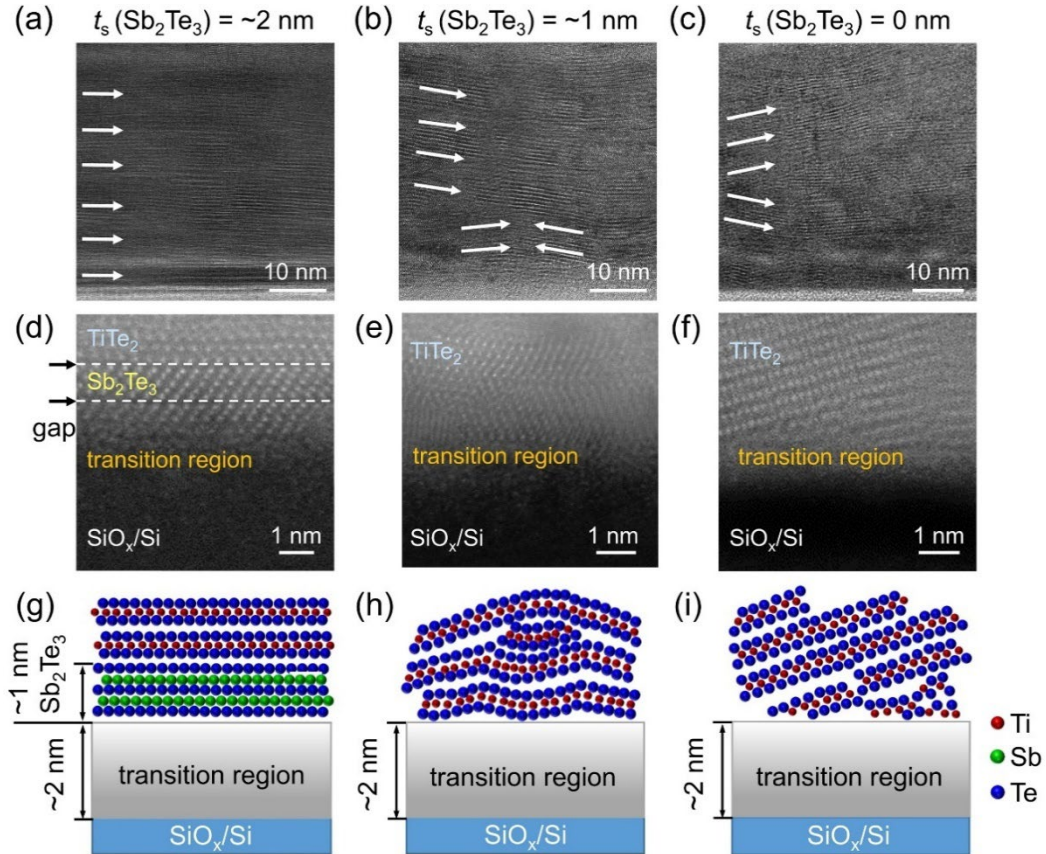


Fig. 6 The critical thickness of the Sb_2Te_3 seed layer. Large-scale HRTEM images of the PCH thin films with Sb_2Te_3 seed layers with a thickness of (a) ~ 2 nm, (b) ~ 1 nm and (c) 0 nm. (d)-(f) Atomic-scale HAADF images of the transition region at the interface with the substrate of the three PCH thin films. (g-i) Sketches of the growth scenarios of the three PCH thin films.

We carried out DFT calculations to gain a better understanding of this phenomenon. As discussed before, the Ar-plasma etching of the silicon substrate leads to an ultrathin amorphous silicon slab with dangling bonds and marginal oxygen at the top edge. We constructed hexagonal supercell models of crystalline TiTe_2 and Sb_2Te_3 and computed the defect formation energy for Si impurities. As shown in Fig. 7, each model contains 60 atoms with 1 Si atom being the substitutional defect, and the cell volume and atomic positions of the models were fully relaxed. We calculated the defect formation energy as $E_d = E_{\text{total}} - E_{\text{pristine}} - E_{\text{Si}} + E_{\text{subst}}$, where E_{total} , E_{pristine} , E_{Si} and E_{subst} represent the energy of the supercell with defect, the pristine phase of the supercell without defect, one Si atom in its bulk ground state, and the one atom being substituted (namely, Ti, Sb or Te atom in their bulk ground state), respectively. For the substitution in the cation sublattice, the E_d value is 2.49 eV to replace one Ti atom with one Si

atom in TiTe_2 and 1.78 eV to replace one Sb atom with one Si atom in Sb_2Te_3 , respectively. To replace one Te atom in the anion sublattice, the E_d value is 1.10 eV for TiTe_2 , and 0.67 eV (edge Te atom) and 1.03 eV (center Te atom) for Sb_2Te_3 , respectively. Clearly, the defect energy to accommodate Si impurities is smaller in Sb_2Te_3 than in TiTe_2 . We also considered models with Si atoms as interstitial defects, which however yielded much too high energy costs as compared to substitutional ones (Fig. S4) and are therefore ruled out. Given the higher substitutional defect energy and the thinner atomic slabs, it is more difficult to form a mixed transition region with TiTe_2 than with Sb_2Te_3 to generate a smooth surface for the subsequent growth of PCH thin film. These calculations are consistent with our experimental observations shown in Fig. 5 and Fig. 6.

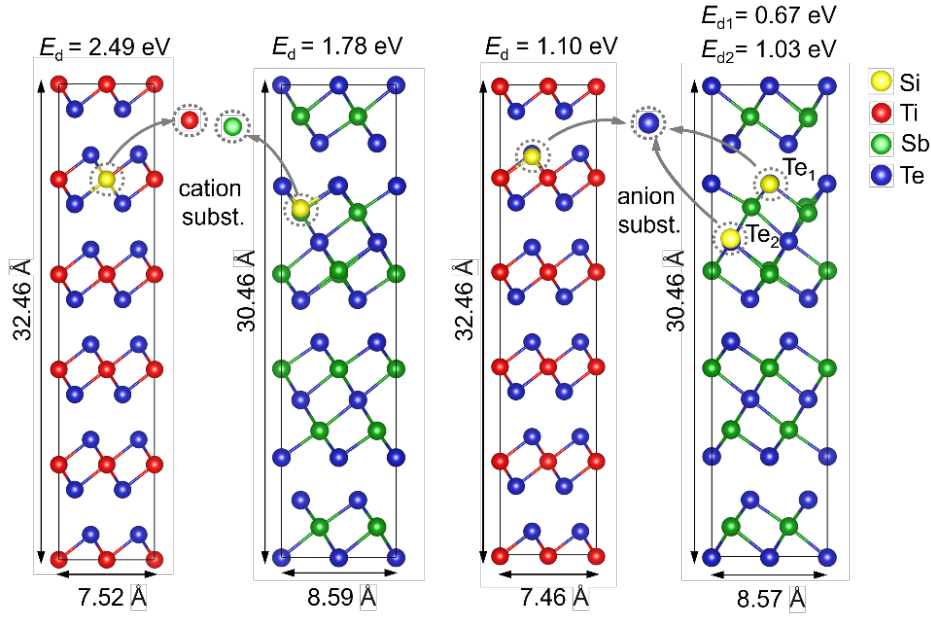


Fig. 7 Defect energy calculations for Si substitution. The Si, Ti, Sb, and Te atoms are rendered as yellow, red, green, and blue spheres, respectively. For Te substitution, two non-equivalent sites were considered, denoted as Te_1 and Te_2 .

It is noted that the defect energy for a Si impurity is lower for Te substitution than for Ti or Sb substitution. To understand this behavior, we carried out charge transfer analyses based on the DFT-calculated wavefunctions [73]. The obtained Löwdin charge distributions of the five supercell models are displayed in Fig. 8, where the charge values of the Si atom are indicated by the black arrows. In the substituted TiTe_2 model, the average charge of Ti atoms is close to 0.6 e, and that of Te atoms is approximately -0.3 e. When the Si atom is incorporated in the Ti sublattice, it tends to gain negative charge rather than to lose it, in contrast to the Ti atoms. This trend becomes more evident for the Te substitution, as the charge of the Si atom reaches -0.6 e. The charge transfer between cation-like Sb and anion-like Te atoms is smaller in Sb_2Te_3 , and the Si atom acquires negative charge for all the three substitutional sites. In short, the Si impurities act as anion-like atoms rather than cation-like atoms in both Sb_2Te_3 and TiTe_2 , owing to the relatively large electronegativity of Si.

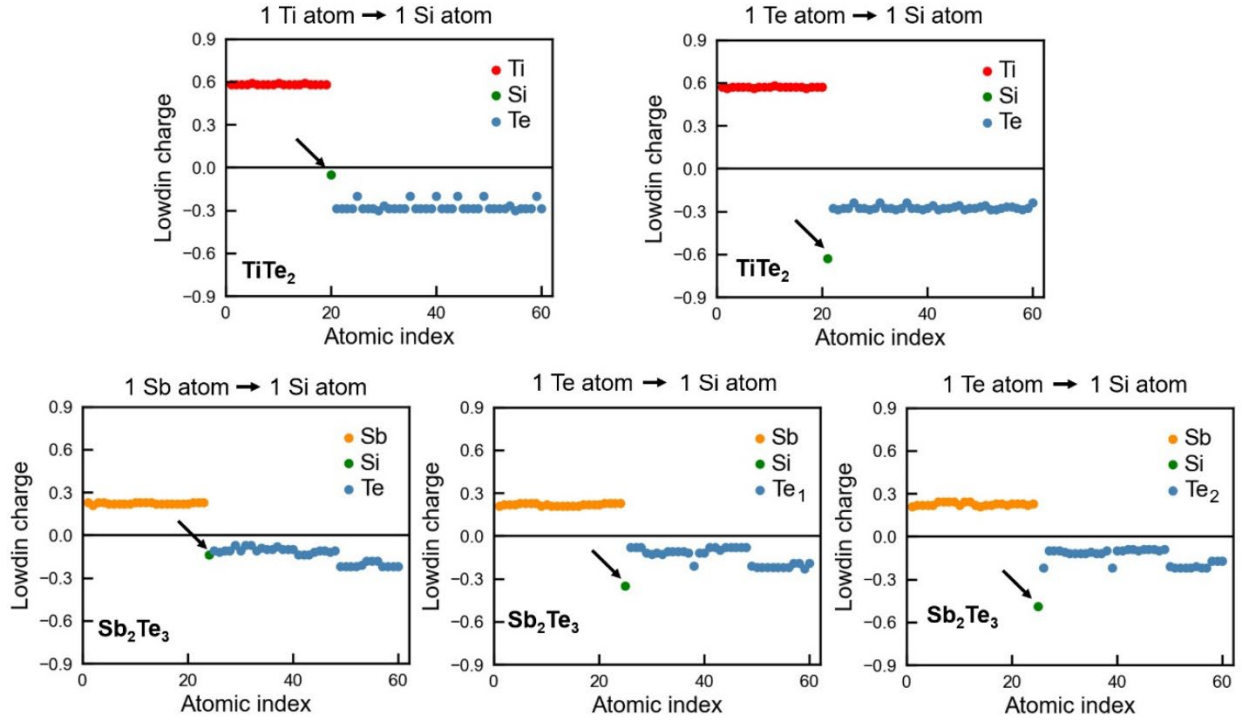


Fig. 8 Löwdin charge analysis. The charge values of Si, Ti, Sb, and Te atoms are depicted with green, red, orange, and blue dots, respectively. The charge values of the Si impurity is marked by a black arrow.

Although it is more frequent to grow Sb_2Te_3 as the seed layer for the high-quality growth of $\text{GeTe}/\text{Sb}_2\text{Te}_3$ superlattice thin films [99-101], it could still be possible to generate a flat interface with the silicon substrate when using TiTe_2 as the seed layer. In a recent work, an IBM team has reported high-quality $\text{TiTe}_2/\text{Sb}_2\text{Te}_3$ growth in a mushroom device with TiTe_2 being the first layer [102], but no details on how to obtain the highly textured seed layer were given. We note that it should be feasible to cover the higher energy costs for mixing TiTe_2 with silicon atoms given a higher annealing temperature or a longer annealing time.

After Ar-plasma etching, Noé *et al.* deposited Sb_2Te_3 directly on heated silicon substrates, which resulted in Te deficiency in the seed layer [103-105]. The Te-poor seed layer could lead to a disorientation by a few degrees of the atomic planes of the $\text{GeTe}/\text{Sb}_2\text{Te}_3$ superlattice with respect to the substrate [103]. Hence, they proposed to increase the concentration of Te for the seed layer growth, and Te-rich layers were clearly captured by HAADF-EDX measurements [105]. This additional compositional tuning can be avoided by heating the substrate after the deposition of the Sb_2Te_3 seed layer is fully completed. Various research teams also reported a complete polishing of the silicon substrates to remove the oxide layers, and epitaxial growth of Sb_2Te_3 , GST and $\text{GeTe}/\text{Sb}_2\text{Te}_3$ thin films was achieved on top of passivated Si(111) surface with a few Sb atomic layers [106-109] or a single Sb/Te atomic layer [110-112]. Nevertheless, full polishing of the native oxide layer adds fabrication costs, and is not necessary if the procedure sketched in Fig. 1a is adopted.

For our approach, the seed layer needs to be chemically unreactive and intact. Therefore, it should be feasible to use Bi_2Te_3 , $\text{Bi}_2\text{Sb}_2\text{Te}_5$ and other GST compositions along the GeTe (SnTe) - Sb_2Te_3 (Bi_2Te_3) pseudo-binary line for the seed layer, as long as a well-ordered trigonal phase can be formed, e.g.,

GeSb₄Te₇, GeSb₂Te₄, Ge₂Sb₂Te₅, Ge₃Sb₂Te₆, Bi₂Te₃, GeBi₂Te₄, SnSb₂Te₄, SnBi₂Te₄, etc. [12, 113-124]. However, the compositions between Ge₈Sb₂Te₁₁ and GeTe may not be good choices as they only form cubic rocksalt-like structure, which could provide reactive surfaces to interact with TiTe₂ layers.

4. Conclusion

In conclusion, we discussed in detail how to achieve epitaxial-like growth of TiTe₂/Sb₂Te₃ thin film at the wafer-scale, with a particular focus on the essential role of the seed layer. By combining atomic-scale structural characterization and *ab initio* modelling, we revealed the underlying growth mechanism yielding an atomically flat Sb₂Te₃ seed layer via a transition slab characterized by a Si-Sb-Te mixture with gradual compositional change. We determined the critical minimum thickness of the seed layer to be ~2 nm with at least one intact ordered Sb₂Te₃ QL block at the top edge. Importantly, *in situ* heating should be avoided during the initial Ar-plasma etching and seed layer growth process, since it promotes the re-formation of SiO₂ on top of the silicon substrate. However, sufficient post annealing of the seed layer is necessary to form well-ordered Sb₂Te₃ QL blocks, prior to the alternate sputtering of the PCH thin film under the *in situ* heating condition. We also observed non-negligible in-plane tensile strain of ~2.4 % in the TiTe₂ blocks induced by the upper and lower Sb₂Te₃ slabs with larger lattice parameters, which indicates that weak covalent coupling is present across the vdW-like gaps in the PCH thin film. The ultrathin Sb₂Te₃ seed layer with critical thickness of ~2 nm could serve as a general starting configuration for highly-textured growth of other chalcogenide thin films at the wafer-scale on a standard silicon substrate with relatively rough SiO_x. We also anticipate further exploration of PCH combinations with alternate stacking of transition metal dichalcogenides as confinement layers and main group chalcogenide semiconductors as memory layers, as long as the latter can form chemically unreactive and intrinsically stable atomic blocks.

Competing interests

The authors declare no competing interests.

Data Availability Statement

Data supporting this work will be available upon requests to the corresponding author.

Acknowledgments

The authors thank the support of XJTU for their work at CAID. W.Z. thanks the support of National Natural Science Foundation of China (62374131). J.-J.W. thanks the support of National Natural Science Foundation of China (62204201). The authors acknowledge Chaobin Zeng from Hitachi High-Tech Scientific Solutions (Beijing) Co., Ltd. and Yuanbin Qin for technical support on STEM experiments. The authors also thank Jia Liu at Instrument Analysis Center of XJTU for the assistance regarding Raman spectroscopy experiments. We acknowledge the HPC platform of XJTU and the Computing Center in Xi'an for providing computational resources. The International Joint Laboratory for Micro/Nano Manufacturing and Measurement Technologies of XJTU is acknowledged. R.M. gratefully acknowledges funding from the PRIN 2020 project “Neuromorphic devices based on chalcogenide heterostructures” funded by the Italian Ministry for University and Research (MUR).

Supplementary materials

Supplementary material associated with this article can be found in the online version at ...

References

- [1] M. Wuttig, N. Yamada, Phase-change materials for rewriteable data storage, *Nat. Mater.* 6, 824-832 (2007).
- [2] W. Zhang, R. Mazzarello, M. Wuttig, E. Ma, Designing crystallization in phase-change materials for universal memory and neuro-inspired computing, *Nat. Rev. Mater.* 4, 150-168 (2019).
- [3] S.W. Fong, C.M. Neumann, H.-S.P. Wong, Phase-Change Memory - Towards a Storage-Class Memory, *IEEE Trans. Electron. Dev.* 64, 4374-4385 (2017).
- [4] A. Sebastian, M. Le Gallo, R. Khaddam-Aljameh, E. Eleftheriou, Memory devices and applications for in-memory computing, *Nat. Nanotechnol.* 15, 529-544 (2020).
- [5] F. Aguirre, A. Sebastian, M. Le Gallo, W. Song, T. Wang, J.J. Yang, W. Lu, M.F. Chang, D. Ielmini, Y. Yang, A. Mehonic, A. Kenyon, M.A. Villena, J.B. Roldan, Y. Wu, H.H. Hsu, N. Raghavan, J. Sune, E. Miranda, A. Eltawil, G. Setti, K. Smagulova, K.N. Salama, O. Krestinskaya, X. Yan, K.W. Ang, S. Jain, S. Li, O. Alharbi, S. Pazos, M. Lanza, Hardware implementation of memristor-based artificial neural networks, *Nat. Commun.* 15, 1974 (2024).
- [6] N. Youngblood, C.A. Ríos Ocampo, W.H.P. Pernice, H. Bhaskaran, Integrated optical memristors, *Nat. Photon.* 17, 561-572 (2023).
- [7] W. Zhou, X. Shen, X. Yang, J. Wang, W. Zhang, Fabrication and integration of photonic devices for phase-change memory and neuromorphic computing, *Int. J. Extrem. Manuf.* 6, 022001 (2024).
- [8] M. Xu, X. Mai, J. Lin, W. Zhang, Y. Li, Y. He, H. Tong, X. Hou, P. Zhou, X. Miao, Recent Advances on Neuromorphic Devices Based on Chalcogenide Phase-Change Materials, *Adv. Funct. Mater.* 30, 2003419 (2020).
- [9] X.D. Li, N.K. Chen, B.Q. Wang, M. Niu, M. Xu, X. Miao, X.-B. Li, Resistive Memory Devices at the Thinnest Limit: Progress and Challenges, *Adv. Mater.* 36, 2307951 (2024).
- [10] B. Liu, K. Li, J. Zhou, Z. Sun, Reversible Crystalline - Crystalline Transitions in Chalcogenide Phase - Change Materials, *Adv. Funct. Mater.* 34, 2407239 (2024).
- [11] N. Yamada, E. Ohno, N. Akahira, K. Nishiuchi, K. Nagata, M. Takao, High Speed Overwritable Phase Change Optical Disk Material, *Jpn. J. Appl. Phys. Part 1* 26, 61-66 (1987).
- [12] N. Yamada, E. Ohno, K. Nishiuchi, N. Akahira, M. Takao, Rapid-phase transitions of GeTe-Sb₂Te₃ pseudobinary amorphous thin films for an optical disk memory, *J. Appl. Phys.* 69, 2849-2856 (1991).
- [13] I. Friedrich, V. Weidenhof, W. Njoroge, P. Franz, M. Wuttig, Structural transformations of Ge₂Sb₂Te₅ films studied by electrical resistance measurements, *J. Appl. Phys.* 87, 4130-4134 (2000).
- [14] B.J. Kooi, J.T.M. De Hosson, Electron diffraction and high-resolution transmission electron microscopy of the high temperature crystal structures of Ge_xSb₂Te_{3+x} (x=1,2,3) phase change material, *J. Appl. Phys.* 92, 3584-3590 (2002).
- [15] B. Zhang, W. Zhang, Z.-J. Shen, Y.-J. Chen, J.-X. Li, S.-B. Zhang, Z. Zhang, M. Wuttig, R. Mazzarello, E. Ma, X.-D. Han, Element-resolved atomic structure imaging of rocksalt Ge₂Sb₂Te₅ phase-change material, *Appl. Phys. Lett.* 108, 191902 (2016).
- [16] T. Siegrist, P. Jost, H. Volker, M. Woda, P. Merkelbach, C. Schlockermann, M. Wuttig, Disorder-induced localization in crystalline phase-change materials, *Nat. Mater.* 10, 202-208 (2011).
- [17] W. Zhang, M. Wuttig, R. Mazzarello, Effects of stoichiometry on the transport properties of crystalline phase-change materials, *Sci. Rep.* 5, 13496 (2015).
- [18] T.-T. Jiang, X.-D. Wang, J.-J. Wang, Y.-X. Zhou, D.-L. Zhang, L. Lu, C.-L. Jia, M. Wuttig, R. Mazzarello, W. Zhang, In situ study of vacancy disordering in crystalline phase-change materials under electron beam irradiation, *Acta Mater.* 187, 103-111 (2020).
- [19] A. Lotnyk, M. Behrens, B. Rauschenbach, Phase change thin films for non-volatile memory applications, *Nanoscale Adv.* 1, 3836-3857 (2019).
- [20] H.-S.P. Wong, S. Raoux, S.B. Kim, J. Liang, J.P. Reifenberg, B. Rajendran, M. Asheghi, K.E. Goodson, Phase Change Memory, *Proc. IEEE* 98, 2201 (2010).

- [21] X. Li, H. Chen, C. Xie, D. Cai, S. Song, Y. Chen, Y. Lei, M. Zhu, Z. Song, Enhancing Performances of Phase Change Memory for Embedded Applications, *Phys. Status Solidi RRL* 13, 1800558 (2019).
- [22] H.Y. Cheng, F. Carta, W.C. Chien, H.L. Lung, M. BrightSky, 3D cross-point phase-change memory for storage-class memory, *J. Phys. D: Appl. Phys.* 52, 473002 (2019).
- [23] P. Cappelletti, R. Annunziata, F. Arnaud, F. Disegni, A. Maurelli, P. Zuliani, Phase change memory for automotive grade embedded NVM applications, *J. Phys. D: Appl. Phys.* 53, 193002 (2020).
- [24] Q. Wang, Y. Wang, Y. Wang, L. Jiang, J. Zhao, Z. Song, J. Bi, L. Zhao, Z. Jiang, J. Schwarzkopf, S. Wu, B. Zhang, W. Ren, S. Song, G. Niu, Long - term and short - term plasticity independently mimicked in highly reliable Ru - doped Ge₂Sb₂Te₅ electronic synapses, *InfoMat* 6, e12543 (2024).
- [25] C. Ríos, M. Stegmaier, P. Hosseini, D. Wang, T. Scherer, C.D. Wright, H. Bhaskaran, W.H.P. Pernice, Integrated all-photonic non-volatile multi-level memory, *Nat. Photon.* 9, 725-732 (2015).
- [26] P. Hosseini, C.D. Wright, H. Bhaskaran, An optoelectronic framework enabled by low-dimensional phase-change films, *Nature* 511, 206-211 (2014).
- [27] W. Zhou, B. Dong, N. Farmakidis, X. Li, N. Youngblood, K. Huang, Y. He, C. David Wright, W.H.P. Pernice, H. Bhaskaran, In-memory photonic dot-product engine with electrically programmable weight banks, *Nat. Commun.* 14, 2887 (2023).
- [28] W. Zhang, R. Mazzarello, E. Ma, Phase-change materials in electronics and photonics, *MRS Bull.* 44, 686-690 (2019).
- [29] D. Ielmini, A.L. Lacaita, D. Mantegazza, Recovery and Drift Dynamics of Resistance and Threshold Voltages in Phase-Change Memories, *IEEE Trans. Electron. Dev.* 54, 308-315 (2007).
- [30] S. Braga, A. Cabrini, G. Torelli, Dependence of resistance drift on the amorphous cap size in phase change memory arrays, *Applied Physics Letters* 94, 092112 (2009).
- [31] M. Boniardi, D. Ielmini, S. Lavizzari, A.L. Lacaita, A. Redaelli, A. Pirovano, Statistics of Resistance Drift Due to Structural Relaxation in Phase-Change Memory Arrays, *IEEE Trans. Electron. Dev.* 57, 2690-2696 (2010).
- [32] M. Boniardi, D. Ielmini, Physical origin of the resistance drift exponent in amorphous phase change materials, *Appl. Phys. Lett.* 98, 243506 (2011).
- [33] A. Sebastian, M. Le Gallo, G.W. Burr, S. Kim, M. BrightSky, E. Eleftheriou, Tutorial: Brain-inspired computing using phase-change memory devices, *J. Appl. Phys.* 124, 111101 (2018).
- [34] M. Le Gallo, A. Sebastian, R. Mathis, M. Manica, H. Giefers, T. Tuma, C. Bekas, A. Curioni, E. Eleftheriou, Mixed-precision in-memory computing, *Nat. Electron.* 1, 246-253 (2018).
- [35] S. Ambrogio, P. Narayanan, H. Tsai, R.M. Shelby, I. Boybat, G.W. Burr, Equivalent-accuracy accelerated neural network training using analogue memory, *Nature* 558, 60-67 (2018).
- [36] J.-Y. Raty, W. Zhang, J. Luckas, C. Chen, C. Bichara, R. Mazzarello, M. Wuttig, Aging mechanisms of amorphous phase-change materials, *Nat. Commun.* 6, 7467 (2015).
- [37] S. Gabardi, S. Caravati, G.C. Sosso, J. Behler, M. Bernasconi, Microscopic origin of resistance drift in the amorphous state of the phase-change compound GeTe, *Phys. Rev. B* 92, 054201 (2015).
- [38] K. Konstantinou, F.C. Mocanu, T.H. Lee, S.R. Elliott, Revealing the intrinsic nature of the mid-gap defects in amorphous Ge₂Sb₂Te₅, *Nat. Commun.* 10, 3065 (2019).
- [39] W. Zhang, E. Ma, Unveiling the structural origin to control resistance drift in phase-change memory materials, *Mater. Today* 41, 156-176 (2020).
- [40] B. Chen, X.P. Wang, F. Jiao, L. Ning, J. Huang, J. Xie, S. Zhang, X.B. Li, F. Rao, Suppressing Structural Relaxation in Nanoscale Antimony to Enable Ultralow-Drift Phase-Change Memory Applications, *Adv. Sci.* 10, 2301043 (2023).
- [41] F. Jiao, B. Chen, K. Ding, K. Li, L. Wang, X. Zeng, F. Rao, Monatomic 2D phase-change memory for precise neuromorphic computing, *Appl. Mater. Today* 20, 100641 (2020).
- [42] P. Ma, H. Tong, M. Xu, X. Cheng, X. Miao, Suppressed resistance drift from short range order of amorphous GeTe ultrathin films, *Appl. Phys. Lett.* 117, 022109 (2020).

- [43] X. Shen, Y. Zhou, H. Zhang, V.L. Deringer, R. Mazzarello, W. Zhang, Surface effects on the crystallization kinetics of amorphous antimony, *Nanoscale* 15, 15259-15267 (2023).
- [44] J. Huang, B. Chen, G. Sha, H. Gong, T. Song, K. Ding, F. Rao, Nanoscale Chemical Heterogeneity Ensures Unprecedentedly Low Resistance Drift in Cache-Type Phase-Change Memory Materials, *Nano Lett.* 23, 2362-2369 (2023).
- [45] B. Liu, K. Li, W. Liu, J. Zhou, L. Wu, Z. Song, S.R. Elliott, Z. Sun, Multi-level phase-change memory with ultralow power consumption and resistance drift, *Sci. Bull.* 66, 2217-2224 (2021).
- [46] Y. Jiao, G. Wang, A. Lotnyk, T. Wu, J. Zhu, A. He, Designing Sb phase change materials by alloying with Ga₂S₃ towards high thermal stability and low resistance drift by bond reconfigurations, *J. Alloys Compd.* 953, 169970 (2023).
- [47] A. He, J. Zhu, G. Wang, A. Lotnyk, S. Cremer, Y. Chen, X. Shen, Development of Sb phase change thin films with high thermal stability and low resistance drift by alloying with Se, *Appl. Phys. Lett.* 124, 221602 (2024).
- [48] T.C. Chong, L.P. Shi, R. Zhao, P.K. Tan, J.M. Li, H.K. Lee, X.S. Miao, A.Y. Du, C.H. Tung, Phase change random access memory cell with superlattice-like structure, *Appl. Phys. Lett.* 88, 122114 (2006).
- [49] R.E. Simpson, P. Fons, A.V. Kolobov, T. Fukaya, M. Krbal, T. Yagi, J. Tominaga, Interfacial phase-change memory, *Nat. Nanotechnol.* 6, 501-505 (2011).
- [50] R. Wang, V. Bragaglia, J.E. Boschker, R. Calarco, Intermixing during Epitaxial Growth of van der Waals Bonded Nominal GeTe/Sb₂Te₃ Superlattices, *Cryst. Growth Des.* 16, 3596-3601 (2016).
- [51] A.V. Kolobov, P. Fons, Y. Saito, J. Tominaga, Atomic Reconfiguration of van der Waals Gaps as the Key to Switching in GeTe/Sb₂Te₃ Superlattices, *ACS Omega* 2, 6223-6232 (2017).
- [52] A. Lotnyk, I. Hilmi, U. Ross, B. Rauschenbach, Van der Waals interfacial bonding and intermixing in GeTe-Sb₂Te₃-based superlattices, *Nano Res.* 11, 1676-1686 (2017).
- [53] L. Zhou, Z. Yang, X. Wang, H. Qian, M. Xu, X. Cheng, H. Tong, X. Miao, Resistance Drift Suppression Utilizing GeTe/Sb₂Te₃ Superlattice-Like Phase-Change Materials, *Adv. Electron. Mater.* 5, 1900781 (2019).
- [54] C. Yoo, J.W. Jeon, B. Park, W. Choi, G. Jeon, S. Jeon, S. Kim, C.S. Hwang, A Review of Advances in Deposition Methods and Material Properties of Superlattice Phase-Change Memory, *ACS Appl. Electron. Mater.* 5, 5794-5808 (2023).
- [55] X.-B. Li, N.-K. Chen, X.-P. Wang, H.-B. Sun, Phase-Change Superlattice Materials toward Low Power Consumption and High Density Data Storage: Microscopic Picture, Working Principles, and Optimization, *Adv. Funct. Mater.* 28, 1803380 (2018).
- [56] B. Sa, J. Zhou, Z. Sun, J. Tominaga, R. Ahuja, Topological insulating in GeTe/Sb₂Te₃ phase-change superlattice, *Phys. Rev. Lett.* 109, 096802 (2012).
- [57] O. Cojocar-Mirédin, J.-C. Bürger, N. Polin, A. Meledin, J. Mayer, M. Wuttig, A. Daus, Thermally Assisted Atomic-Scale Intermixing and Ordering in GeTe-Sb₂Te₃ Superlattices, *ACS nano* DOI: 10.1021/acsnano.4c13450 (2025).
- [58] K. Ding, J. Wang, Y. Zhou, H. Tian, L. Lu, R. Mazzarello, C. Jia, W. Zhang, F. Rao, E. Ma, Phase-change heterostructure enables ultralow noise and drift for memory operation, *Science* 366, 210-215 (2019).
- [59] J. Shen, S. Lv, X. Chen, T. Li, S. Zhang, Z. Song, M. Zhu, Thermal Barrier Phase Change Memory, *ACS Appl. Mater. Interfaces* 11, 5336-5343 (2019).
- [60] X. Wang, K. Ding, M. Shi, J. Li, B. Chen, M. Xia, J. Liu, Y. Wang, J. Li, E. Ma, Z. Zhang, H. Tian, F. Rao, Unusual phase transitions in two-dimensional telluride heterostructures, *Mater. Today* 54, 52-62 (2022).
- [61] X. Wang, Y. Wu, Y. Zhou, V.L. Deringer, W. Zhang, Bonding nature and optical contrast of TiTe₂/Sb₂Te₃ phase-change heterostructure, *Mater. Sci. Semicond. Process.* 135, 106080 (2021).
- [62] G. Han, F. Liu, Y. Zhang, J. Li, W. Li, Q. Chen, Y. Li, X. Xie, Effect of structure architecture on optical properties of TiTe₂/Sb₂Te₃ multilayer nanofilms, *J. Alloys Compd.* 877, 160270 (2021).
- [63] J. Park, H. Sung, S. Son, S. Ju, H. Lee, Sb₂Te₃/TiTe₂-Heterostructure-Based Phase Change Memory for Fast Set Speed and Low Reset Energy, *Phys. Status Solidi RRL* 17, 2200451 (2023).
- [64] R. Piombo, S. Ritarossi, R. Mazzarello, Ab Initio Study of Novel Phase - Change Heterostructures, *Adv. Sci.* 11, 2402375

(2024).

- [65] T.H. Kim, S.W. Park, H.J. Lee, D.H. Kim, J.Y. Choi, T.G. Kim, Effect of Transition Metal Dichalcogenide Based Confinement Layers on the Performance of Phase-Change Heterostructure Memory, *Small* 19, 2303659 (2023).
- [66] T.H. Kim, K.J. Yoo, T.H. Kim, H.J. Lee, A.C. Khot, K.A. Nirmal, S.H. Hong, T.G. Kim, Enhancement of thermal stability and device performances through XTe₂/TaxSb₂Te₃-based phase-change heterostructure, *Appl. Surf. Sci.* 626, 157291 (2023).
- [67] S.W. Park, H.J. Lee, K.A. Nirmal, T.H. Kim, D.H. Kim, J.Y. Choi, J.S. Oh, J.M. Joo, T.G. Kim, Phase-change heterostructure with HfTe₂ confinement sublayers for enhanced thermal efficiency and low-power operation through Joule heating localization, *J. Mater. Sci. Technol.* 204, 104-114 (2025).
- [68] X. Wu, A.I. Khan, H. Lee, C.-F. Hsu, H. Zhang, H. Yu, N. Roy, A.V. Davydov, I. Takeuchi, X. Bao, H.S.P. Wong, E. Pop, Novel nanocomposite-superlattices for low energy and high stability nanoscale phase-change memory, *Nat. Commun.* 15, 13 (2024).
- [69] G. Kresse, J. Hafner, Ab initio molecular dynamics for liquid metals, *Phys. Rev. B* 47, 558-561 (1993).
- [70] J.P. Perdew, K. Burke, M. Ernzerhof, Generalized gradient approximation made simple, *Phys. Rev. Lett.* 77, 3865-3868 (1996).
- [71] G. Kresse, D. Joubert, From ultrasoft pseudopotentials to the projector augmented-wave method, *Phys. Rev. B* 59, 1758 (1999).
- [72] S. Grimme, J. Antony, S. Ehrlich, H. Krieg, A consistent and accurate ab initio parametrization of density functional dispersion correction (DFT-D) for the 94 elements H-Pu, *J. Chem. Phys.* 132, 154104 (2010).
- [73] R. Nelson, C. Ertural, J. George, V.L. Deringer, G. Hautier, R. Dronskowski, LOBSTER: Local orbital projections, atomic charges, and chemical-bonding analysis from projector-augmented-wave-based density-functional theory, *J. Comput. Chem.* 41, 1931-1940 (2020).
- [74] S. Maintz, V.L. Deringer, A.L. Tchougreff, R. Dronskowski, LOBSTER: A tool to extract chemical bonding from plane-wave based DFT, *J. Comput. Chem.* 37, 1030-1035 (2016).
- [75] V.L. Deringer, A.L. Tchougreff, R. Dronskowski, Crystal orbital Hamilton population (COHP) analysis as projected from plane-wave basis sets, *J. Phys. Chem. A* 115, 5461-5466 (2011).
- [76] Y. Saito, P. Fons, A.V. Kolobov, J. Tominaga, Self-organized van der Waals epitaxy of layered chalcogenide structures, *Phys. Status Solidi B* 252, 2151-2158 (2015).
- [77] Y. Saito, P. Fons, L. Bolotov, N. Miyata, A.V. Kolobov, J. Tominaga, A two-step process for growth of highly oriented Sb₂Te₃ using sputtering, *AIP Adv.* 6, 045220 (2016).
- [78] Y. Saito, P. Fons, A.V. Kolobov, K.V. Mitrofanov, K. Makino, J. Tominaga, S. Hatayama, Y. Sutou, M. Hase, J. Robertson, High-quality sputter-grown layered chalcogenide films for phase change memory applications and beyond, *J. Phys. D: Appl. Phys.* 53, 284002 (2020).
- [79] T.L. Anderson, H.B. Krause, Refinement of the Sb₂Te₃ and Sb₂Te₂Se structures and their relationship to nonstoichiometric Sb₂Te₃-ySey compounds, *Acta Crystallogr. B* 30 1307-1310 (1974).
- [80] Y. Zheng, M. Xia, Y. Cheng, F. Rao, K. Ding, W. Liu, Y. Jia, Z. Song, S. Feng, Direct observation of metastable face-centered cubic Sb₂Te₃ crystal, *Nano Res.* 9, 3453-3462 (2016).
- [81] Y. Xu, X. Wang, W. Zhang, L. Schäfer, J. Reindl, F. vom Bruch, Y. Zhou, V. Evang, J.J. Wang, V.L. Deringer, E. Ma, M. Wuttig, R. Mazzarello, Materials Screening for Disorder-Controlled Chalcogenide Crystals for Phase-Change Memory Applications, *Adv. Mater.* 33, 2006221 (2021).
- [82] W. Richter, C.R. Becker, A Raman and far - infrared investigation of phonons in the rhombohedral V₂-VI₃ compounds Bi₂Te₃, Bi₂Se₃, Sb₂Te₃ and Bi₂(Te_{1-x}Sex)₃ (0<x<1), (Bi_{1-y}Sby)₂Te₃ (0<y<1), *Phys. Status Solidi B* 84, 619-628 (1977).
- [83] K.M.F. Shahil, M.Z. Hossain, V. Goyal, A.A. Balandin, Micro-Raman spectroscopy of mechanically exfoliated few-quintuple layers of Bi₂Te₃, Bi₂Se₃, and Sb₂Te₃ materials, *J. Appl. Phys.* 111, 054305 (2012).
- [84] G.C. Sosso, S. Caravati, M. Bernasconi, Vibrational properties of crystalline Sb₂Te₃ from first principles, *J. Phys.*

Condens. Matter. 21, 095410 (2009).

- [85] X. Feng, Z. Li, G. Chen, H. Yue, Y. Gao, X. Zhang, Z. Guo, W. Yuan, Single-crystal growth of layered metallic materials of TiTe₂ based on a polytelluride flux method, *CrystEngComm* 25, 5399-5404 (2023).
- [86] S.J. Pennycook, P.D. Nellist, Scanning Transmission Electron Microscopy Imaging and Analysis, Springer 2011.
- [87] R. Wang, F.R.L. Lange, S. Cecchi, M. Hanke, M. Wuttig, R. Calarco, 2D or Not 2D: Strain Tuning in Weakly Coupled Heterostructures, *Adv. Funct. Mater.* 28, 1705901 (2018).
- [88] J. Wang, I. Ronneberger, L. Zhou, L. Lu, V.L. Deringer, B. Zhang, L. Tian, H. Du, C. Jia, X. Qian, M. Wuttig, R. Mazzarello, W. Zhang, Unconventional two-dimensional germanium dichalcogenides, *Nanoscale* 10, 7363-7368 (2018).
- [89] Y. Cheng, O. Cojocaru-Miréidin, J. Keutgen, Y. Yu, M. Küpers, M. Schumacher, P. Golub, J.-Y. Raty, R. Dronskowski, M. Wuttig, Understanding the Structure and Properties of Sesqui-Chalcogenides (i.e., V₂VI₃ or Pn₂Ch₃ (Pn = Pnictogen, Ch = Chalcogen) Compounds) from a Bonding Perspective, *Adv. Mater.* 31, 1904316 (2019).
- [90] J.Y. Raty, M. Schumacher, P. Golub, V.L. Deringer, C. Gatti, M. Wuttig, A Quantum-Mechanical Map for Bonding and Properties in Solids, *Adv. Mater.* 31, 1806280 (2019).
- [91] B.J. Kooi, M. Wuttig, Chalcogenides by Design: Functionality through Metavalent Bonding and Confinement, *Adv. Mater.* 32, 1908302 (2020).
- [92] M. Wuttig, C.F. Schon, J. Lotfering, P. Golub, C. Gatti, J.Y. Raty, Revisiting the Nature of Chemical Bonding in Chalcogenides to Explain and Design their Properties, *Adv. Mater.* 35, 2208485 (2023).
- [93] M. Wuttig, C.F. Schon, D. Kim, P. Golub, C. Gatti, J.Y. Raty, B.J. Kooi, A.M. Pendas, R. Arora, U. Waghmare, Metavalent or Hypervalent Bonding: Is There a Chance for Reconciliation?, *Adv. Sci.* 11, 2308578 (2023).
- [94] W. Zhang, H. Zhang, S. Sun, X. Wang, Z. Lu, X. Wang, J.-J. Wang, C. Jia, C.F. Schon, R. Mazzarello, E. Ma, M. Wuttig, Metavalent Bonding in Layered Phase-Change Memory Materials, *Adv. Sci.* 10, 2300901 (2023).
- [95] M. Chhowalla, H.S. Shin, G. Eda, L.J. Li, K.P. Loh, H. Zhang, The chemistry of two-dimensional layered transition metal dichalcogenide nanosheets, *Nat. Chem.* 5, 263-275 (2013).
- [96] J. Qi, X. Qian, L. Qi, J. Feng, D. Shi, J. Li, Strain-engineering of band gaps in piezoelectric boron nitride nanoribbons, *Nano Lett.* 12, 1224-8 (2012).
- [97] J. Li, Z. Shan, E. Ma, Elastic strain engineering for unprecedented materials properties, *MRS Bull.* 39, 108-114 (2014).
- [98] W. Li, X. Qian, J. Li, Phase transitions in 2D materials, *Nat. Rev. Mater.* 6, 829-846 (2021).
- [99] J. Momand, F.R.L. Lange, R. Wang, J.E. Boschker, M.A. Verheijen, R. Calarco, M. Wuttig, B.J. Kooi, Atomic stacking and van-der-Waals bonding in GeTe–Sb₂Te₃ superlattices, *J. Mater. Res.* 31, 3115-3124 (2016).
- [100] A.I. Khan, A. Daus, R. Islam, K.M. Neilson, H.R. Lee, H.-S.P. Wong, E. Pop, Ultralow-switching current density multilevel phase-change memory on a flexible substrate, *Science* 373, 1243-1247 (2021).
- [101] S. Prili, V. Bragaglia, V.P. Jonnalagadda, J. Luchtenveld, B.J. Kooi, F. Arciprete, A. Sebastian, G.S. Syed, Understanding the Growth and Properties of Sputter-Deposited Phase-Change Superlattice Films, *arXiv: 2411.19343* (2024).
- [102] G.M. Cohen, A. Majumdar, C.W. Cheng, A. Ray, D. Piatek, L. Gignac, C. Lavoie, A. Grun, H.Y. Cheng, Z.L. Liu, H.L. Lung, H. Miyazoe, R.L. Bruce, M. BrightSky, Low RESET Current Mushroom - Cell Phase - Change Memory Using Fiber - Textured Homostructure GeSbTe on Highly Oriented Seed Layer, *Phys. Status Solidi RRL* 18, 2300426 (2024).
- [103] P. Kowalczyk, F. Hippert, N. Bernier, C. Mocuta, C. Sabbione, W. Batista - Pessoa, P. Noé, Impact of Stoichiometry on the Structure of van der Waals Layered GeTe/Sb₂Te₃ Superlattices Used in Interfacial Phase-Change Memory (iPCM) Devices, *Small* 14, 1704514 (2018).
- [104] F. Hippert, P. Kowalczyk, N. Bernier, C. Sabbione, X. Zucchi, D. Térébénec, C. Mocuta, P. Noé, Growth mechanism of highly oriented layered Sb₂Te₃ thin films on various materials, *J. Phys. D: Appl. Phys.* 53, 154003 (2020).
- [105] V. Sever, N. Bernier, D. Térébénec, C. Sabbione, J. Paterson, F. Castioni, P. Quéméré, A. Jannaud, J.L. Rouvière, H. Roussel, J.Y. Raty, F. Hippert, P. Noé, Quantitative Scanning Transmission Electron Microscopy-High-Angle-Annular Dark - Field Study of the Structure of Pseudo - 2D Sb₂Te₃ Films Grown by (Quasi) Van der Waals Epitaxy, *Phys. Status Solidi RRL*

18, 2300402 (2024).

[106] J. Momand, R. Wang, J.E. Boschker, M.A. Verheijen, R. Calarco, B.J. Kooi, Interface formation of two- and three-dimensionally bonded materials in the case of GeTe-Sb₂Te₃ superlattices, *Nanoscale* 7, 19136-19143 (2015).

[107] R. Wang, R. Calarco, F. Arciprete, V. Bragaglia, Epitaxial growth of GeTe/Sb₂Te₃ superlattices, *Mater. Sci. Semicond. Process.* 137, 106244 (2022).

[108] V. Bragaglia, F. Arciprete, W. Zhang, A.M. Mio, E. Zallo, K. Perumal, A. Giussani, S. Cecchi, J.E. Boschker, H. Riechert, S. Privitera, E. Rimini, R. Mazzarello, R. Calarco, Metal-Insulator Transition Driven by Vacancy Ordering in GeSbTe Phase Change Materials, *Sci. Rep.* 6, 23843 (2016).

[109] V. Bragaglia, F. Arciprete, A.M. Mio, R. Calarco, Designing epitaxial GeSbTe alloys by tuning the phase, the composition, and the vacancy ordering, *J. Appl. Phys.* 123, (2018).

[110] I. Hilmi, A. Lotnyk, J.W. Gerlach, P. Schumacher, B. Rauschenbach, Research Update: Van-der-Waals epitaxy of layered chalcogenide Sb₂Te₃ thin films grown by pulsed laser deposition, *APL Materials* 5, 050701 (2017).

[111] M. Behrens, A. Lotnyk, U. Roß, J. Griebel, P. Schumacher, J.W. Gerlach, B. Rauschenbach, Impact of disorder on optical reflectivity contrast of epitaxial Ge₂Sb₂Te₅ thin films, *CrystEngComm* 20, 3688-3695 (2018).

[112] H. Bryja, J.W. Gerlach, A. Prager, M. Ehrhardt, B. Rauschenbach, A. Lotnyk, Epitaxial layered Sb₂Te₃ thin films for memory and neuromorphic applications, *2D Materials* 8, 045027 (2021).

[113] J.-W. Park, S.H. Eom, H. Lee, J.L.F. Da Silva, Y.-S. Kang, T.-Y. Lee, Y.H. Khang, Optical properties of pseudobinary GeTe, Ge₂Sb₂Te₅, GeSb₂Te₄, GeSb₄Te₇, and Sb₂Te₃ from ellipsometry and density functional theory, *Phys. Rev. B* 80, 115209 (2009).

[114] J. Da Silva, A. Walsh, H. Lee, Insights into the structure of the stable and metastable (GeTe)_m(Sb₂Te₃)_n compounds, *Phys. Rev. B* 78, 224111 (2008).

[115] Z. Sun, Y. Pan, J. Zhou, B. Sa, R. Ahuja, Origin of p-type conductivity in layered nGeTe-mSb₂Te₃ chalcogenide semiconductors, *Phys. Rev. B* 83, 113201 (2011).

[116] Y. Gan, J. Zhou, Z. Sun, Prediction of the atomic structure and thermoelectric performance for semiconducting Ge₁Sb₆Te₁₀ from DFT calculations, *J. Mater. Inf.* 1, 2 (2021).

[117] Y. Gan, Y. Huang, N. Miao, J. Zhou, Z. Sun, Novel IV-V-VI semiconductors with ultralow lattice thermal conductivity, *J. Mater. Chem. C* 9, 4189-4199 (2021).

[118] J.J. Wang, H.M. Zhang, X.D. Wang, L. Lu, C. Jia, W. Zhang, R. Mazzarello, In - Plane Twinning Defects in Hexagonal GeSb₂Te₄, *Adv. Mater. Technol.* 7, 2200214 (2022).

[119] J.-J. Wang, J. Wang, H. Du, L. Lu, P.C. Schmitz, Johannes Reindl, A.M. Mio, C.-L. Jia, E. Ma, R. Mazzarello, M. Wuttig, W. Zhang, Genesis and Effects of Swapping Bilayers in Hexagonal GeSb₂Te₄, *Chem. Mater.* 30, 4770-4777 (2018).

[120] H. Zhang, D.T. Yimam, S. de Graaf, J. Momand, P.A. Vermeulen, Y. Wei, B. Noheda, B.J. Kooi, Strain Relaxation in "2D/2D and 2D/3D Systems": Highly Textured Mica/Bi₂Te₃, Sb₂Te₃/Bi₂Te₃, and Bi₂Te₃/GeTe Heterostructures, *ACS nano* 15, 2869-2879 (2021).

[121] H. Zhang, J. Momand, J. Levinsky, Q. Guo, X. Zhu, G.H. ten Brink, G.R. Blake, G. Palasantzas, B.J. Kooi, Nanostructure and thermal power of highly-textured and single-crystal-like Bi₂Te₃ thin films, *Nano Res.* 15, 2382-2390 (2021).

[122] D. Hsieh, Y. Xia, D. Qian, L. Wray, F. Meier, J. Dil, J. Osterwalder, L. Patthey, A. Fedorov, H. Lin, A. Bansil, D. Grauer, Y. Hor, R. Cava, M. Hasan, Observation of Time-Reversal-Protected Single-Dirac-Cone Topological-Insulator States in Bi₂Te₃ and Sb₂Te₃, *Phys. Rev. Lett.* 103, 146401 (2009).

[123] S. Howard, A. Raghavan, D. Iaia, C. Xu, D. Flötotto, M.-H. Wong, S.-K. Mo, B. Singh, R. Sankar, H. Lin, T.-C. Chiang, V. Madhavan, Observation of a smoothly tunable Dirac point in Ge(BixSb1-x)₂Te₄, *Phys. Rev. Mater.* 6, 044201 (2022).

[124] T. Schäfer, P.M. Konze, J.D. Huyeng, V.L. Deringer, T. Lesieur, P. Müller, M. Morgenstern, R. Dronskowski, M. Wuttig, Chemical Tuning of Carrier Type and Concentration in a Homologous Series of Crystalline Chalcogenides, *Chem. Mater.* 29, 6749-6757 (2017).

Supporting Information

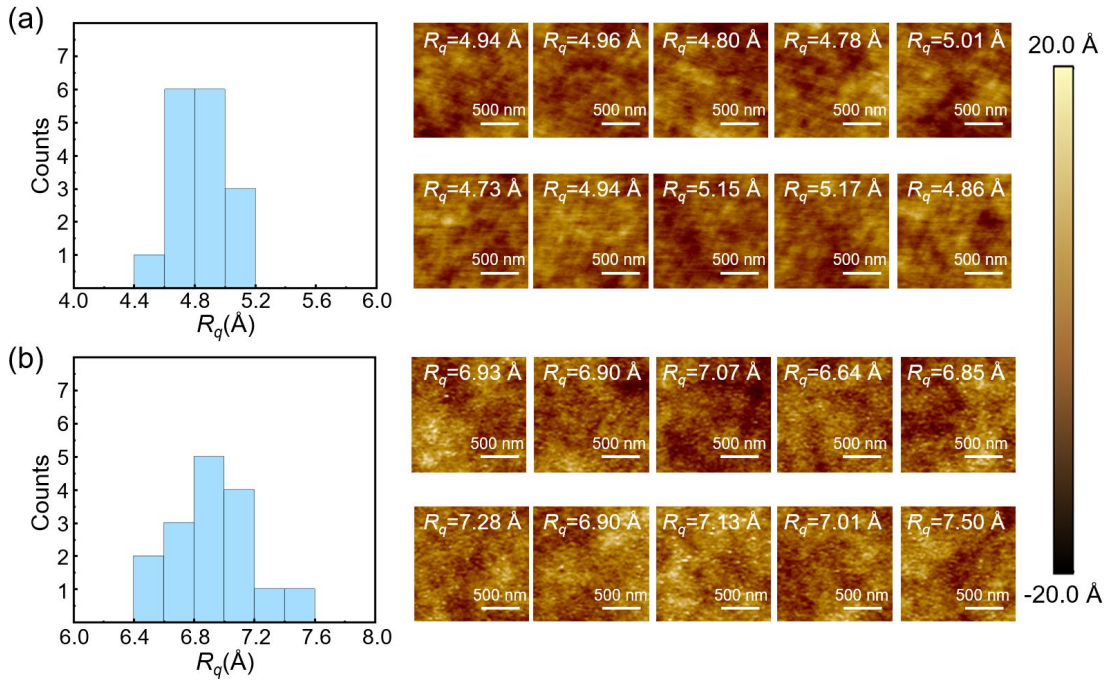


Fig. S1 Statistical histogram of the root-mean-square roughness R_q for 16 different regions, and the AFM images for ten of them. (a) ~5nm thick Sb_2Te_3 seed layer and (b) ~45nm thick $\text{Sb}_2\text{Te}_3/\text{TiTe}_2$ film. The R_q of Sb_2Te_3 seed layer and $\text{Sb}_2\text{Te}_3/\text{TiTe}_2$ film are observed to be below 5.2 Å and 7.6 Å, respectively.

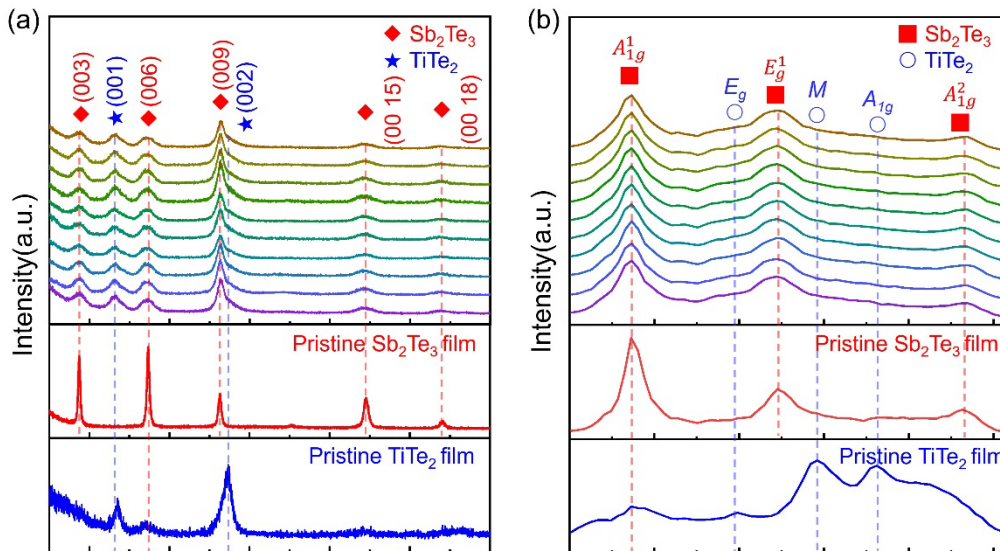


Fig. S2 (a) XRD patterns and (b) Raman spectra for ten different sampling spots in $\text{Sb}_2\text{Te}_3/\text{TiTe}_2$ thin films.

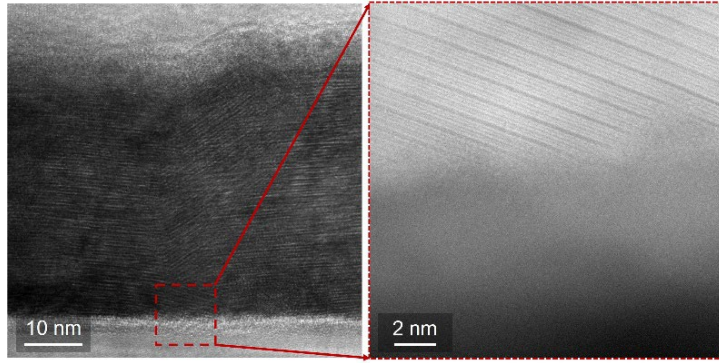


Fig. S3 The TEM characterizations of the $\text{TiTe}_2/\text{Sb}_2\text{Te}_3$ thin film, for which the growth of the Sb_2Te_3 seed layer was also subjected to in situ heating condition.

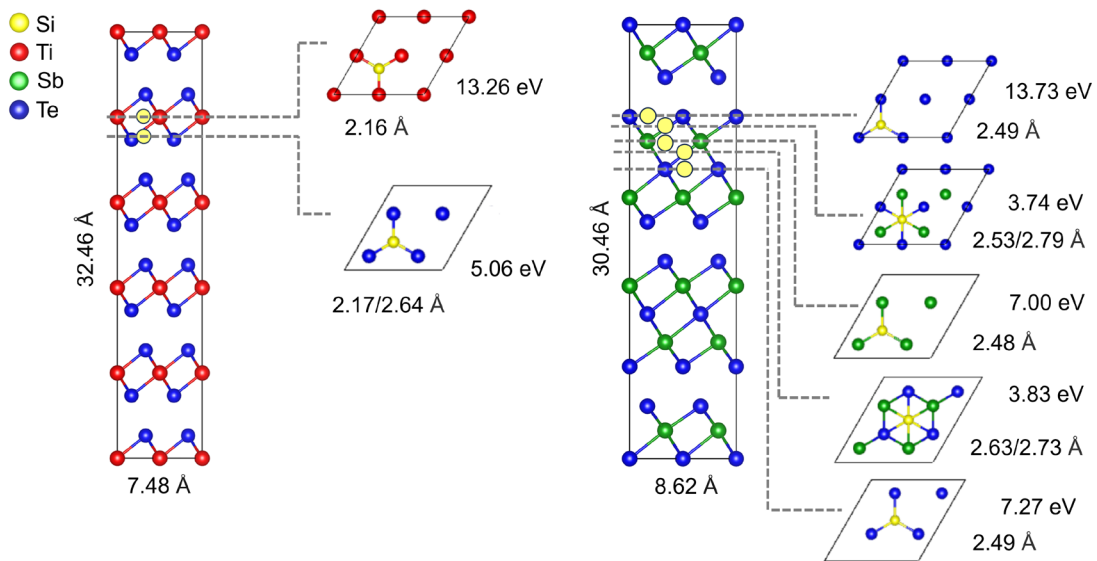


Fig. S4 Defect formation energy (E_d) of Si interstitial sites. The E_d value is calculated as $E_d = E_{\text{total}} - E_{\text{pristine}} - E_{\text{Si}}$, where E_{total} , E_{pristine} and E_{Si} represent the energy of the supercell with one interstitial Si atom, the pristine phase of the supercell, and the energy of one Si atom in its bulk ground state. The Si, Ti, Sb, and Te atoms are rendered as yellow, red, green, and blue spheres, respectively. The Si interstitial atom adds much higher energy costs, and would induce large atomic displacement of the surrounding atoms upon relaxation.